

pubs.acs.org/JPCC Article

# Exfoliation of Quasi-Two-Dimensional Nanosheets of Metal Diborides

Ahmed Yousaf,<sup>‡</sup> Matthew S. Gilliam,<sup>‡</sup> Shery L. Y. Chang, Mathias Augustin, Yuqi Guo, Fraaz Tahir, Meng Wang, Alexandra Schwindt, Ximo S. Chu, Duo O. Li, Suneet Kale, Abhishek Debnath, Yongming Liu, Matthew D. Green, Elton J. G. Santos,\* Alexander A. Green,\* and Qing Hua Wang\*



Cite This: J. Phys. Chem. C 2021, 125, 6787-6799



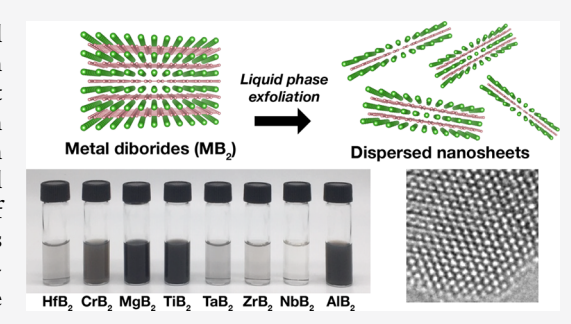
ACCESS

Metrics & More

Article Recommendations

s Supporting Information

ABSTRACT: Metal diborides are a class of ceramic materials with crystal structures consisting of hexagonal sheets of boron atoms alternating with planes of metal atoms held together with mixed character ionic/covalent bonds. Many of the metal diborides are ultrahigh-temperature ceramics such as HfB<sub>2</sub>, TaB<sub>2</sub>, and ZrB<sub>2</sub>, which have melting points above 3000 °C, high mechanical hardness and strength at high temperatures, and high chemical resistance, while MgB<sub>2</sub> is a superconductor with a transition temperature of 39 K. Here, we demonstrate that this diverse family of non-van der Waals (vdW) materials can be processed into stable dispersions of quasi-two-dimensional (2D) nanosheets using ultrasonication-assisted exfoliation. We generate quasi-2D nanosheets of the metal diborides AlB<sub>2</sub>, CrB<sub>2</sub>, HfB<sub>2</sub>, MgB<sub>2</sub>,



NbB<sub>2</sub>, TaB<sub>2</sub>, TiB<sub>2</sub>, and ZrB<sub>2</sub> and use electron and scanning probe microscopy techniques to characterize their structures, morphologies, and compositions. The exfoliated layers have a distribution of lateral dimensions from tens of nanometers up to several micrometers and a distribution of thicknesses from as low as 2–3 nm up to tens of nanometers, all while retaining their hexagonal atomic structure and chemical composition. We exploit the convenient solution-phase dispersions of exfoliated CrB<sub>2</sub> nanosheets to incorporate them directly into polymer composites. In contrast to the hard and brittle bulk CrB<sub>2</sub>, we find that CrB<sub>2</sub> nanocomposites remain very flexible and simultaneously provide increases in the elastic modulus and the ultimate tensile strength of the polymer. The successful liquid-phase production of quasi-2D metal diborides enables their processing using scalable low-temperature solution-phase methods, extending their use to previously unexplored applications, and reveals a new family of non-vdW materials that can be efficiently exfoliated into quasi-2D forms.

## INTRODUCTION

Metal diborides are a family of ceramic compounds with the general formula MB2, where M can be a variety of metals from Groups II, IVB, and VB such as Hf, Cr, Ti, Zr, Mg, and so forth. The most common crystal structure of these materials is the AlB<sub>2</sub> type, belonging to the P6/mmm space group symmetry, which has the boron atoms in covalently bound hexagonal sheets separated by layers of close-packed metal atoms, as shown in Figure 1A. The interactions between the alternating layers of metal atoms and boron atoms have a mixed ionic and covalent character. Depending on the identity of the metal atoms, the M-B and B-B bond lengths and bonding strengths vary, leading to dramatic compositiondependent differences in properties.<sup>2,3</sup> Metal diborides exhibit a diverse range of remarkable physical properties. 1,4-6 For example, several of them have very high melting points, including some that exceed 3000 °C, such as HfB2 and ZrB2 which are considered ultrahigh-temperature ceramics (UHTCs). 1,7,8 Other examples of remarkable properties exhibited by the metal diborides include high mechanical strength and hardness (Young's modulus above 480 GPa for ZrB<sub>2</sub> and HfB<sub>2</sub>), exceptional mechanical performance at temperatures above 1500 °C for ZrB<sub>2</sub> ceramics, high thermal conductivity, resistance to chemical attack, high electrical conductivity, and electrocatalytic activity for the hydrogen evolution reaction. In contrast, MgB<sub>2</sub> has a substantially lower melting temperature of 830 °C but is well known as a superconductor with a transition temperature of 39 K, which ranks among the highest of the conventional superconductors. Transition temperature of superconductors.

These properties make UHTC metal diboride materials suitable for extreme conditions, with applications such as high-temperature electrodes, coatings in cutting tools, neutron absorption in nuclear reactors, armor, and components for

Received: January 15, 2021 Revised: March 8, 2021 Published: March 22, 2021





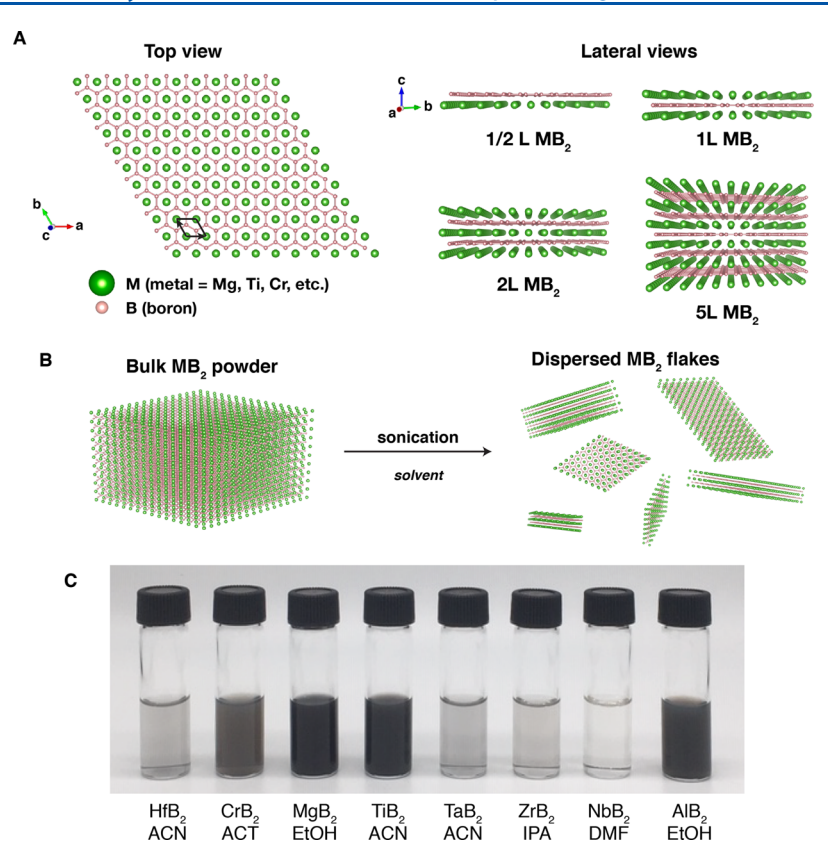


**Figure 1.** Structure and dispersions of metal diborides. (A) Structure of metal diborides in top view and lateral views of different layer thicknesses. One unit cell with **a** and **b** axes is outlined in the top view. (B) Schematic illustration of exfoliation process employed to disperse metal diborides in solvents via sonication. (C) Photograph of vials of metal diboride dispersions in various organic solvents: HfB<sub>2</sub>, TiB<sub>2</sub>, and TaB<sub>2</sub> in ACN, CrB<sub>2</sub> in ACT, MgB<sub>2</sub> and AlB<sub>2</sub> in EtOH, ZrB<sub>2</sub> in IPA, and NbB<sub>2</sub> in DMF.

hypersonic flight and atmospheric reentry vehicles. <sup>1,7,20</sup> However, these ceramic materials have been mostly limited to uses as rigid structures. Furthermore, processing of metal diborides usually requires methods such as high-temperature sintering and pressing, <sup>21</sup> sintering with various additives, <sup>22,23</sup> and spark plasma sintering, <sup>24,25</sup> but the densification of UHTC metal diborides, which is required for aerospace and nuclear applications, is difficult due to their high melting temperatures. <sup>21</sup> Thus, new methods of processing for metal diborides have the potential to greatly expand the range of applications for these materials, enabling their exceptional properties to be fully exploited. In recent years, metal diborides along with other boron-based compounds have been gaining renewed attention from chemists, who have been studying their electrochemical properties and potential for alternative low-temperature and solution-based processing routes. <sup>26–34</sup>

The layered structure of metal diborides with their graphene-like boron sheets suggests the possibility of exfoliation into thin nanosheets. The ability to produce metal diborides as quasi-two dimensional (2D) nanosheets using mild processing conditions could provide an attractive new route to applying these materials and extending their use to new contexts. Despite this potential, efforts to produce nanosheets of metal diborides have so far been focused mainly on the superconducting MgB<sub>2</sub> rather than any of the UHTC materials and yielded chemically modified products that have different structures, stoichiometries, and chemical functionalities compared to their bulk source materials. For example, Das et al. produced hydroxyl-functionalized and Mg-deficient few-layer B-based sheets by sonicating bulk MgB<sub>2</sub> powder in

water.<sup>31</sup> The same group followed up with some other strategies for producing highly modified nanosheets including chelation-assisted exfoliation utilizing ethylenediamine tetraacetic acid, which removes much of the Mg metal and adds hydride, hydroxyl, and oxy-functional groups to the remaining B-based layers;<sup>34</sup> ionic liquid-assisted exfoliation in 1-butyl-3methyl-imidazolium tetrafluoroborate;<sup>33</sup> and treatment with sulfuric acid followed by intercalation with organoammonium ions.<sup>32</sup> Nishino et al. similarly showed that sonication of MgB<sub>2</sub> in water produces hydroxyl-functionalized Mg-deficient boron nanosheets<sup>35</sup> and that the reaction of MgB<sub>2</sub> with an ion exchange resin in an acetonitrile (ACN) solution produces hydrogen boride.<sup>36</sup> For the other metal diborides besides MgB<sub>2</sub>, Lim et al. treated TiB<sub>2</sub> with butyllithium and sodium naphthalenide but were unsuccessful in its exfoliation.<sup>27</sup> Thus, to our knowledge, a successful method to produce unmodified few-layer 2D forms of the family of metal diborides has not been reported.

Here, we report the efficient exfoliation of the family of metal diboride compounds into unmodified few-layer nanosheets using direct liquid-phase exfoliation. Using ultrasonication in suitable solvents, we successfully exfoliated eight different metal diboride compounds—AlB<sub>2</sub>, CrB<sub>2</sub>, HfB<sub>2</sub>, MgB<sub>2</sub>, NbB<sub>2</sub>, TaB<sub>2</sub>, TiB<sub>2</sub>, and ZrB<sub>2</sub>—to prepare liquid-phase dispersions with concentrations up to 2.4 mg mL<sup>-1</sup>. We use density functional theory (DFT) calculations to demonstrate that the metal diborides MgB<sub>2</sub> and HfB<sub>2</sub> are stable in few-layer-thick quasi-2D forms and to simulate their electron-energy-loss spectroscopy (EELS) spectra. Transmission electron microscopy (TEM) imaging of the resulting dispersions confirms the

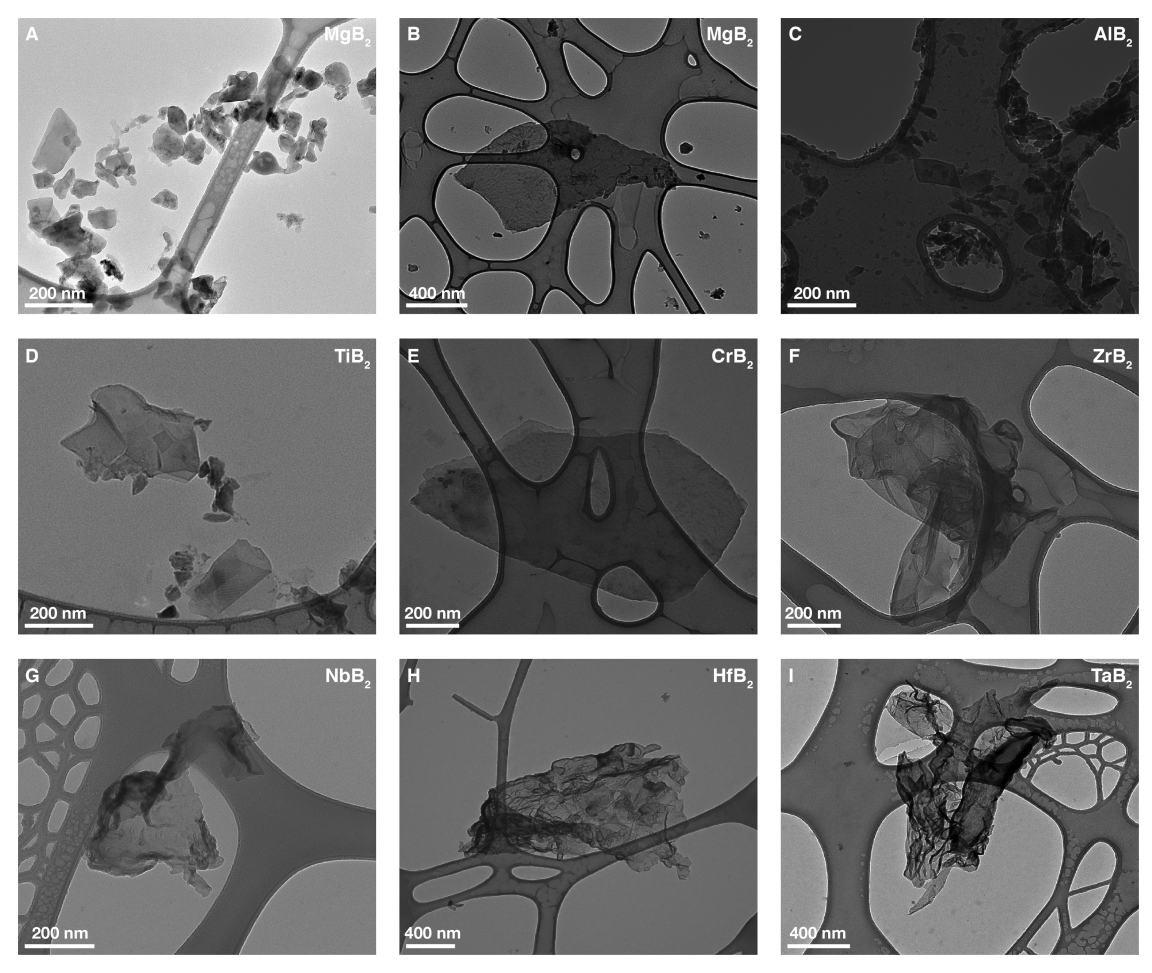


Figure 2. TEM imaging of metal diboride flakes. (A–I) Low-magnification TEM images of flakes from eight different metal diboride compounds generated by solution-phase dispersions (tip-sonicated except CrB<sub>2</sub> and MgB<sub>2</sub> bath-sonicated). Lateral dimensions of flakes range from 30 nm to 2  $\mu$ m.

2D nature of the nanosheets and reveals that their hexagonal structure is retained after exfoliation. Atomic force microscopy (AFM) of the nanosheets shows a distribution of thicknesses ranging from 2-3 nm at the thinnest to a few tens of nanometers. Furthermore, EELS spectra obtained from the metal diboride nanosheets demonstrate that the chemical composition is maintained after the exfoliation process. Finally, we employ our direct exfoliation approach to prepare dispersions of nanosheets of chromium diboride (CrB<sub>2</sub>) directly in aqueous solutions of polyvinyl alcohol (PVA), which enables facile production of metal diboride-reinforced polymer composites. The resulting CrB<sub>2</sub>/PVA composites provide improvements in elastic modulus (E) and ultimate tensile strength (UTS) of up to 23 and 48%, respectively, over the polymer alone. These results introduce a new family of normally brittle metal diboride ceramics that are amenable to scalable, low-temperature solution-phase processing, thus enabling their use in flexible, conformal, and stretchable forms.

## METHODS

**Materials.** All chemicals were used as received without further purification. MgB<sub>2</sub>, AlB<sub>2</sub>, TiB<sub>2</sub>, NbB<sub>2</sub>, TaB<sub>2</sub>, PVA with a molecular weight of 89,000–98,000 g/mol, N,N-dimethylformamide (DMF), and 1-methyl-2-pyrrolidinone (NMP) were purchased from Sigma-Aldrich, CrB<sub>2</sub> from Alfa Aesar, and ZrB<sub>2</sub>

and  $HfB_2$  from Smart Elements. More details of the materials and chemicals are listed in the Supporting Information.

Preparation of Metal Diboride Dispersions. For tip sonication, 0.4 g of each metal diboride powder was added to a 15 mL centrifuge tube along with 6 mL of the organic solvent. Then, the mixture was tip-sonicated (Branson Digital Sonifier 450D, 3 mm diameter tip) for 1 h at 20% amplitude corresponding to 11-13 W of power output. For bath sonication, 0.4 g of each metal diboride powder was mixed in 6 mL organic solvent in centrifuge tubes and bath-sonicated at full power for variable times in the range of 4-8 h, in ice water (Branson CPX2800H). The resulting dispersions from either tip or bath sonication were transferred into 1.75 mL tubes and centrifuged at 5000 RCF for 4 min, and then the top 1 mL of the dispersion was extracted. We note that MgB<sub>2</sub> has a higher dispersion efficiency than the other metal diborides so we sometimes used a lower starting amount (0.2 g) to conserve material, but it is still greatly in excess of the resulting dispersed nanosheets, and higher centrifugation speed (10,000 RCF) is needed to remove more of the larger, thicker particles and aggregates. The comparisons of dispersions in Figure S1 were for samples prepared under identical conditions.

The concentrations of each dispersion were measured by inductively coupled mass spectrometry (ICP-MS).

Tip sonication was used for initial screening experiments to see which combinations of metal diboride compositions and

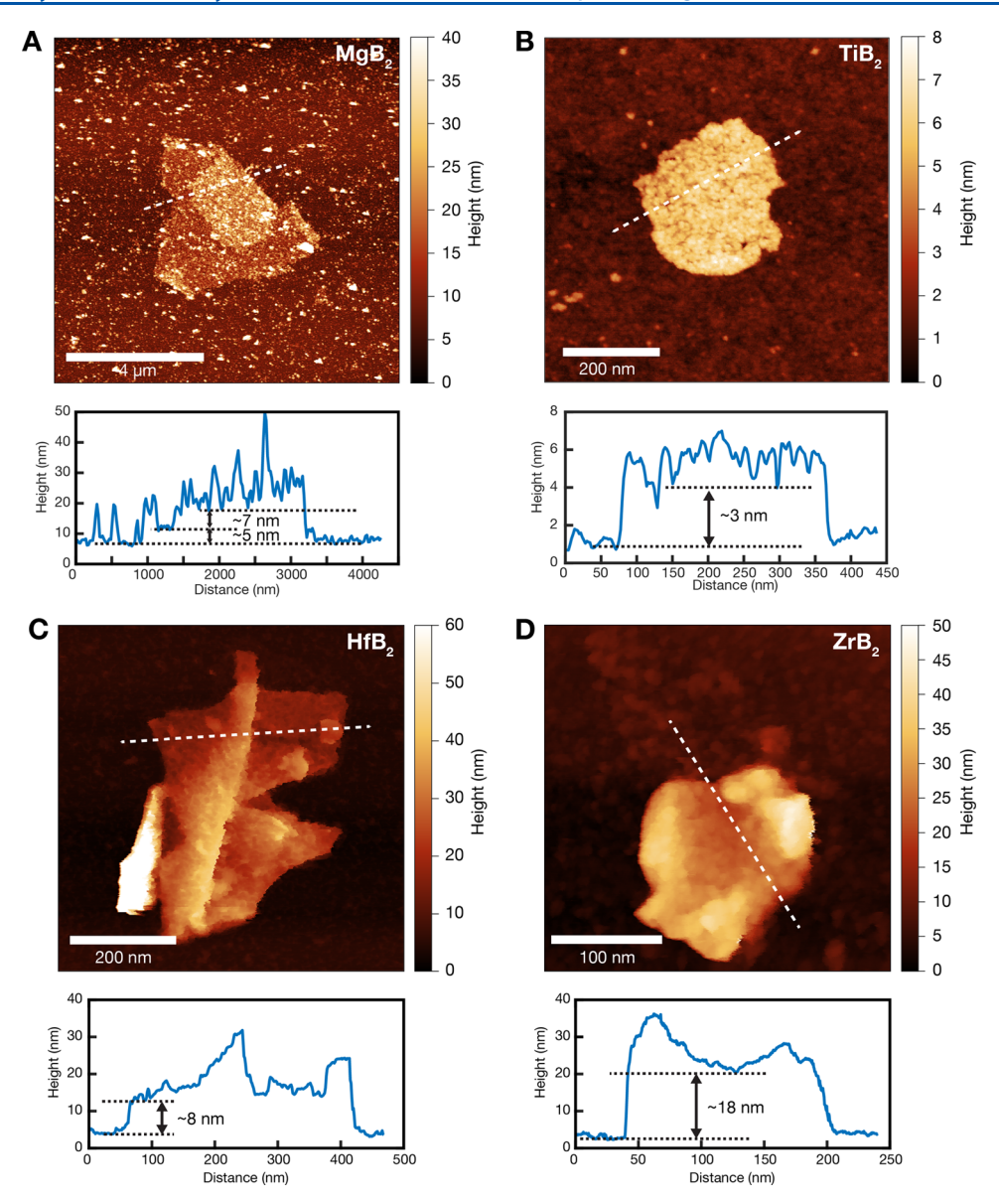


Figure 3. AFM imaging of metal diboride flakes. (A) MgB<sub>2</sub> flake dispersed by bath sonication in IPA, deposited onto the  $SiO_2/Si$  substrate, and imaged in air. (B)  $TiB_2$  flake dispersed by bath sonication in IPA, deposited onto the  $SiO_2/Si$  substrate, and imaged in air. (C)  $HfB_2$  flake dispersed by tip sonication in IPA, deposited on the mica substrate, and imaged in air. (D)  $TrB_2$  flake dispersed by tip sonication in IPA, deposited on the  $SiO_2/Si$  substrate, and imaged in water. Height profiles along the dashed lines are shown below each AFM image.

solvents would lead to successful dispersions because we hypothesized that the higher and more concentrated sonication power of tip sonication would be needed to break apart the metal diborides, which are more strongly held together than van der Waals (vdW) materials. We then tried bath sonication and found that it was also able to exfoliate the nanosheets. However, we did not find any significant differences between the tip- or bath-sonicated nanosheets. Thus, there are results from both tip and bath sonication reported in this work.

**ICP-MS.** For each dispersion, a 50  $\mu$ L aliquot was acidified overnight in 2 mL of concentrated nitric acid following by a dilution of the matrix to 2 wt % of HNO<sub>3</sub> aqueous solution. The concentration was determined by ICP-MS (iCap Q quadrupole, Thermo Fisher).

**Optical Extinction Spectroscopy.** The dispersions were diluted as needed, and the corresponding solvent was used as the reference. The UV-vis-NIR spectra were collected from

 $400\ to\ 1000\ nm$  in quartz cuvettes using a Jasco V-670 spectrophotometer.

**TEM.** TEM images in Figure 2 and Figure S2 were acquired on a Philips CM 12 at 80 kV, and aberration-corrected high-resolution transmission electron microscopy (HRTEM) images in Figure 3 and Figure S3 were obtained on a FEI aberration-corrected Titan at 300 kV. The images were taken under negative  $C_s$  imaging conditions, where the spherical aberration is tuned to about  $-14~\mu m$ . To determine lattice spacings, the peak positions for each atom within the flakes were fitted first, and then least-squares criteria were used to refine the lattice spacings of all equivalent  $\{100\}$  planes in the flake. This over-redundant measurement method improves the accuracy of the measurement for small flakes. Flakes with well-defined edges and that were easily distinguished were identified, and their areas were measured using ImageJ. The histograms of their areas are shown in Figure S4.

EDS and EELS. EDS spectra were also collected on a Titan. EELS was performed on an ARM 200F equipped with an Enfinium spectrometer operated at 200 kV and also 80 kV. The lower voltage was used to avoid electron beam damage to the thin boride layers. The B K-edge was taken using a dispersion of 0.1 eV/ch, whereas the Hg M-edge and Mg M-edge were 1 eV/ch. The EELS elemental relative quantification was carried out using the Gatan Microscopy Suite (GMS) software, using the formula

$$\frac{N_{\rm A}}{N_{\rm B}} = \frac{I_{\rm A}\sigma_{\rm B}}{I_{\rm B}\sigma_{\rm A}}$$

where N is the areal density of a specific element and I is the integrated intensity under the specific edge and  $\sigma$  is the partial cross section.

The edges and the intensity of the edge for the flakes were optimized to minimize the systematic and statistical error while not damaging the flakes during the acquisition.

The edges we chose to quantify are the B K-edge and Hf M-edge, which are both within a suitable energy loss region (< 2000 eV). As the flakes are very thin, the effects of plural scattering and plasmons are negligible and therefore have little impact on the quantification. Moreover, there are no other elements present before the B K-edge, and the Hf M-edge is in the higher energy range, so background subtraction and the potential influence from the tails of other elements are not present. The major error source of this measurement is the cross section of the M edge as M edges typically have higher errors of about 20%.

AFM. AFM imaging was carried out on a Multimode V system (Bruker Corp.) with ScanAsyst-Air tips (Bruker) in ScanAsyst noncontact mode. Gwyddion<sup>37</sup> was used for image processing. Dispersions of HfB2, ZrB2, and TiB2 were prepared in isopropanol (IPA) using the tip or bath sonication methods as described above. Substrates were either freshly cleaved mica or SiO<sub>2</sub>/Si wafers cleaned by sonication in acetone (ACT) then IPA for 5 min each and blown dry using ultrapure nitrogen. A drop of each dispersion was spin-coated on each substrate at 2500-3000 rpm for 1 min. Spin coating was repeated two to five times to increase the areal concentration of nanosheets. Prior to AFM imaging, the samples were annealed at 300 °C for 9 h to remove organic residues. Some imaging was also performed in liquid using Bruker ScanAsyst-Fluid+ probes and by depositing a 50 µL droplet of ultrapure water on the sample and immersing the probe; no significant differences in flake morphologies were observed in liquid versus air imaging. Processed images were then used to identify flakes, measure their height profiles using Gywddion to obtain thicknesses, and measure their areas using ImageJ. Histograms of the thickness and area of flakes were then plotted.

**Polymer Composite Preparation.** To synthesize composites with PVA, 1.3 g of chromium diboride was bath-sonicated in 20 mL of 1% w/v aqueous PVA solution for 10 h, and the resulting suspension was distributed equally in 1.75 mL tubes and centrifuged at 5000 rcf for 5 min. Control solutions of PVA alone were processed using identical conditions. To further concentrate the CrB<sub>2</sub> in PVA, the CrB<sub>2</sub> dispersions were centrifuged to pellet out the CrB<sub>2</sub> nanosheets, half of the supernatant was removed, and the pelleted nanosheets were redispersed in the remaining PVA solution with shaking and bath sonication. The concentration of the resulting dispersion was determined by ICP-MS and used along with UV-vis-NIR

measurements to calculate the extinction coefficient for CrB<sub>2</sub> dispersed in 1% PVA. The mass loadings of the composites were then determined using the calculated extinction coefficient and UV-vis measurements. The CrB<sub>2</sub>/PVA dispersions were mixed with appropriate amounts of 1% w/v aqueous PVA solution containing no CrB2 by vortexing to obtain the required CrB2 mass loadings, and then the mixtures were bath-sonicated for 20 min. Afterwards, 24 mL of the resulting mixtures were poured into Petri dishes and dried in an oven at 60 °C for 48 h under vacuum. The dried CrB<sub>2</sub>/PVA membranes were peeled from the Petri dishes, cut into rectangular pieces of roughly 5 cm × 1 cm, and taped at the edges such that the working length was 3 cm. The average thickness of each film was calculated from three measurements along the length of each film and used for tensile stress calculations. These films were then subjected to tensile testing. The same procedure was also used for PVA blank controls without adding any nanomaterials.

**Tensile Testing.** The mechanical behavior of the CrB<sub>2</sub>/PVA composites was characterized by tensile testing of the 3 cm × 1 cm rectangular strips prepared as described above. The tests were conducted on an Instron E3000 Test Instrument with a 1 kN load cell and self-aligning grips. The stress was calculated from the load cell reading and the initial cross-sectional area of each specimen. The strain was calculated from crosshead displacement. All test specimens were stretched at a constant crosshead speed of 0.5 mm/s. At least three specimens were tested for each nanosheet concentration. Because the stress—strain curves do not have a clearly linear region, the elastic modulus was calculated by applying a linear least-squares fit to different small regions of the stress—strain curve and finding the maximum slope for each sample.

X-ray Diffraction (XRD). Powders of exfoliated MgB<sub>2</sub> were prepared by bath sonicating batches of 1.3 g amounts of MgB<sub>2</sub> in 20 mL aliquots of IPA for approximately 2 h. The resultant mixtures were then distributed into 1.75 mL microcentrifuge tubes and centrifuged for 10 min at 5000 rcf to remove large aggregates, isolating the nanosheets within the supernatant. The supernatant containing nanosheets was then collected and subjected to additional centrifugation such that the nanosheets within the dispersion pelleted out almost completely. The supernatant of the spun down nanosheets was removed, and 200 µL was added to the pelleted nanosheets to redisperse them. This process was repeated many times to concentrate the nanosheets within one solution. The concentrated solution was finally spun down, the supernatant was removed, and the pellet was left to dry overnight in an oven to obtain the powder used for powder x-ray diffraction (PXRD). The ZrB<sub>2</sub> powder was prepared similarly, except that instead of bath sonication, tip sonication was used (2 h, 35% amplitude) on batches of 1.3 g of ZrB<sub>2</sub> in 22 mL of IPA. Bulk powders of MgB<sub>2</sub> and ZrB<sub>2</sub> were used as received. For the PXRD measurements, films of the powders were prepared on quartz substrates by placing powders onto the middle of the substrate and spraying IPA on both sides to allow the powders to soak up the solvent and spread across the substrate. After drying, PXRD spectra of the films were collected on a Siemens D5000 Powder X-ray diffractometer at a scan rate of 3 degrees per minute using copper K- $\alpha$  radiation.

Nanocomposite PVA films containing different loadings of  $CrB_2$  nanosheets, along with a film of PVA alone, were prepared as described earlier for mechanical testing of samples. The films were then taped by the edges to a quartz substrate to

collect PXRD spectra. Bulk CrB<sub>2</sub> powder was analyzed using a film prepared as above for the MgB<sub>2</sub> and ZrB<sub>2</sub> powders. As an additional control, a PXRD spectrum of the quartz substrate with no polymer or powder film was also collected.

Fourier Transform Infrared (FTIR) Spectroscopy. Transmittance FTIR measurements were performed on powder samples obtained from centrifugation-based concentration and drying similar to those prepared for PXRD measurements. Samples were analyzed with a Nicolet 6700 FTIR with 64 scans taken for each sample and 128 scans taken for a background measurement in air. Within the OMNIC software used to collect the spectra, transmittance measurements were converted to absorbance measurements, and a baseline correction was applied to each spectrum before conversion back to transmittance spectra.

**DFT Calculations.** The calculations were performed using the plane-wave basis set within the DFT with the Vienna Ab-Initio Simulation Package (VASP) package. 38,39 We used the Perdew–Burke–Ernzerhof (PBE) functional 40,41 with the projector augmented wave pseudopotentials. 42,43 We used the DFT-D3 corrections to describe vdW interactions. 44 A 500 eV plane-wave cutoff was used, and the systems were relaxed until the forces on the atoms were less than 0.0001 eV/Å. The Brillouin zone was sampled with a Monkhorst-Pack of  $15 \times 15$ × 15 k-points in the bulk unit cell, whose equivalent grid was utilized on the layered systems. We used Phonopy<sup>45</sup> to compute the phonon dispersion spectra for the 1 L, 2 L, and bulk MgB<sub>2</sub>. The EELS spectra were computed with CASTEP<sup>46</sup> using the optimized geometries from the calculations with VASP and on on-the-fly generated pseudopotential with PBE functionals. A k-grid of 21 × 21 × 1 k-points for all layers and  $21 \times 21 \times 21$  for the bulk was used in CASTEP. The energy cutoff was 600 eV.

**Statistical Information.** Error bars in the mechanical properties in Figure 5 were calculated from the standard deviations of n = 3 samples for each value.

## RESULTS

Exfoliation of MB<sub>2</sub> Nanosheets. Few-layer metal diboride nanosheets were prepared using ultrasonication in several solvents, as schematically illustrated in Figure 1B. Ultrasonication relies on the principle of cavitation to shear apart the sheets, which are then stabilized by the surrounding solvent molecules. Bulk powders of each of the metal diborides were added to solvents and sonicated using a tip or bath ultrasonicator (see further details in the Methods section). Following centrifugation to remove poorly dispersed materials, the supernatant was decanted. This process was applied to eight different metal diborides for which powder source materials were available: aluminum diboride (AlB<sub>2</sub>), chromium diboride (CrB<sub>2</sub>), hafnium diboride (HfB<sub>2</sub>), magnesium diboride (MgB<sub>2</sub>), niobium diboride (NbB<sub>2</sub>), tantalum diboride (TaB<sub>2</sub>), titanium diboride (TiB<sub>2</sub>), and zirconium diboride (ZrB<sub>2</sub>). Tip sonication was first used because it can generate more concentrated sonication power for exfoliating these nonvdW materials, but bath sonication was subsequently used and was also found to be effective. Some of the data shown below are from tip-sonicated materials, and some are from bath-sonicated; while we found the nanosheets produced by both methods to be quite similar, bath sonication was more reliable and had higher overall throughput because multiple vials of samples could be processed simultaneously.

The resulting solution-phase dispersions were gray to black in appearance. Figure 1C shows a photograph of dispersions of the different metal diborides prepared in different solvents by bath sonication. The optical extinction spectra, which are a combination of absorption and scattering, obtained from the dispersions are mostly featureless with the exception of MgB<sub>2</sub>, which shows two broad peaks near 400 and 850 nm as shown in the Supporting Information, Figure S1a. The concentrations of the metal diboride liquid-phase dispersions were determined using ICP-MS. We used ICP-MS to determine the concentrations of the dispersions because it is more accurate for lower concentrations as we have for the metal diborides, has been used in previous studies of 2D material dispersions, 47-49 and does not require as much mass as gravimetric methods for an accurate assessment. These measurements showed a broad range of concentrations from 2.4 mg/mL for MgB<sub>2</sub> to 0.07 mg/mL for ZrB<sub>2</sub> (Supporting Information, Figure S1b). These values are comparable to the concentrations reported for previous studies of the most widely studied 2D materials based on vdW solids, such as graphene, BN, and transition-metal dichalcogenides. 50-53 Different solvents were found to be more effective for dispersing some metal diboride compositions than others. The dispersions shown in the photograph in Figure 1C are obtained using a solvent, which resulted in the highest concentrations for each composition: HfB2, TiB2, and TaB2 were in ACN, CrB2 in ACT, MgB2 and AlB2 in ethanol (EtOH), ZrB2 in IPA, and NbB<sub>2</sub> in DMF. The variation in dispersion concentrations for different combinations of metal diboride compositions is seen in the plot of the resulting concentrations (Figure S1b). An example of the extinction coefficient is shown in Figure S13, and a plot of the stability of dispersions over two weeks' time is shown in Figure S14. Many of the dispersions are stable in suspension for weeks without precipitating, while some precipitated after a few days. We have conducted a separate study of the dispersion of metal diboride nanosheets in a wide range of different solvents and use Hansen solubility theory to explain the variations of exfoliation efficiency.<sup>54</sup>

Structural Characterization of MB<sub>2</sub> Nanosheets. To confirm the 2D nature of the sheets, TEM images were obtained for all eight metal diborides (Figure 2). The flakes are found in different morphologies varying from flat, planar sheets, as shown for the MgB2, AlB2, TiB2, and CrB2, to folded and crumpled ones, as shown for ZrB<sub>2</sub>, NbB<sub>2</sub>, HfB<sub>2</sub>, and TaB<sub>2</sub>. The flake sizes were found to vary, with AlB<sub>2</sub> having the smallest flakes (< 100 nm across) and MgB<sub>2</sub> the largest up to several microns across. Additional TEM images are shown in the Supporting Information, Figure S2. Histograms of the areas of HfB2 and MgB2 flakes from TEM images were plotted and are shown in the Supporting Information, Figure S4. We observe a decrease in the average flake area with longer centrifugation times. We note that there is variable morphology (i.e., flat, folded, and wrinkled) across the same compositions, which we attribute to the liquid-phase exfoliation process and the deposition and drying of dispersions on TEM grids. Similar variations in morphology have been seen in TEM images of liquid-phase-exfoliated nanosheets of other compositions in the literature. 51,55-57

AFM was used to characterize the thicknesses and areas of nanosheets of MgB<sub>2</sub>, TiB<sub>2</sub>, HfB<sub>2</sub>, and ZrB<sub>2</sub> (Figure 3). Samples of metal diboride nanosheets were prepared by both tip sonication and bath sonication and deposited by spin coating onto SiO<sub>2</sub>/Si and mica substrates (see the Methods section for

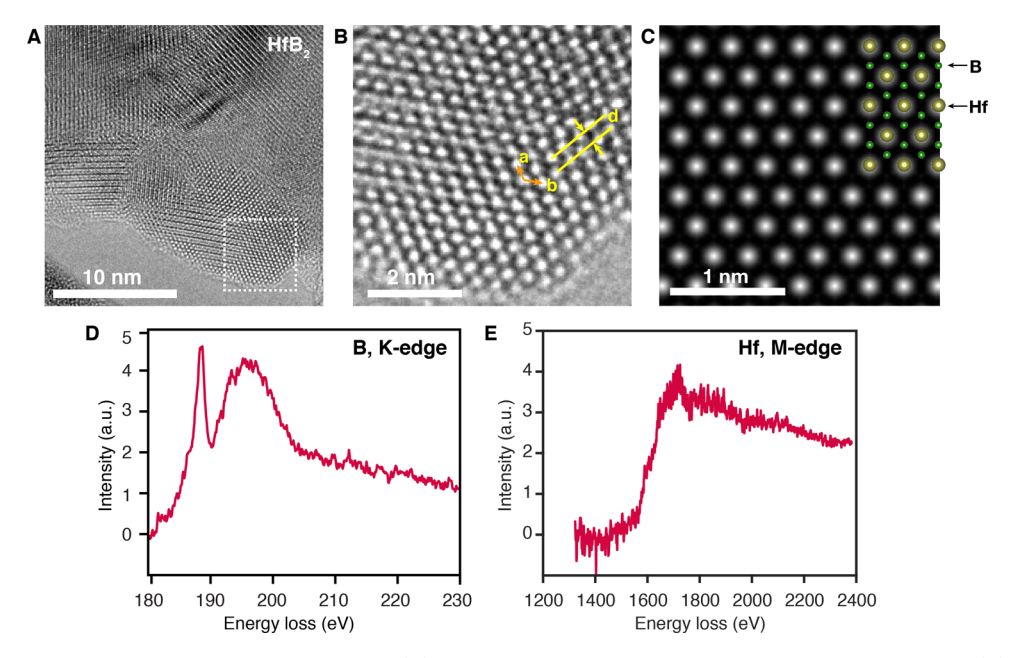


Figure 4. HRTEM and EELS characterization of HfB<sub>2</sub> flakes. (A) Aberration-corrected TEM imaging of HfB<sub>2</sub> of 4-5 layers. (B) Enlarged image of the area marked by a square in (A), with the arrows depicting the basis vectors of the hexagonal structure of HfB<sub>2</sub>. The parallel lines indicate the (100) planes, which have a spacing of 2.68 Å. (C) Simulated HRTEM image of 4 layers of HfB<sub>2</sub> based on the bulk crystal structure, with HfB<sub>2</sub> structure overlaid. (D) and (E) EELS spectra of HfB<sub>2</sub>, with the B K-edge in (D) and the Hf M-edge in (E). Nanosheets were dispersed by tip sonication.

more details). Both types of substrates were used and found to be similar in performance; the mica is a bit smoother than the SiO<sub>2</sub>/Si, but the latter is better for optical imaging of nanosheets because of the optical interference of the 300 nm thick oxide layer. Spin coating was used rather than drop casting to avoid the formation of aggregates. We found that this process in general resulted in flakes of a smaller lateral area to be deposited onto the substrate compared to those observed in TEM imaging, but larger areas could be obtained from a less aggressive bath sonication treatment to reduce the likelihood of sonication-induced cutting. We also note that there may be some differences in what flakes get captured during the imaging processes because it is easier to take large-area scans in TEM to find larger flakes than in AFM, where scan sizes are much more limited. AFM images in Figure 3 show flakes of different sizes and varying thicknesses. Height profiles show typical thicknesses ranging from about 3 to 18 nm and lateral dimensions of about 150 nm to 4 µm across. Given the interlayer spacing of 0.35 nm for bulk crystalline HfB2, ZrB2, and MgB<sub>2</sub><sup>28</sup> and assuming a hydration layer of 0.35 to 1.5 nm thickness on the outer surface of the flakes, 58-60 these nanosheets are about 8-50 layers thick. Additional AFM images of the sample areas surrounding these flakes with more flakes of various sizes are shown in the Supporting Information, Figure S3. Histograms of the areas and thicknesses of HfB2 and MgB<sub>2</sub> flakes were plotted and are shown in the Supporting Information, Figure S5. Generally, thicker flakes have larger areas, and we achieve much thinner flakes for MgB<sub>2</sub> than HfB<sub>2</sub>, with a significant proportion of flakes thinner than 5 nm.

XRD was also conducted according to the details described in the Methods section for the exfoliated  $MgB_2$ ,  $ZrB_2$ , and  $CrB_2$  and compared to their corresponding initial bulk powders, as shown in the Supporting Information, Figure S8. The main diffraction peaks are almost entirely absent in the exfoliated materials, indicating that they have lost their stacking order.

To elucidate the atomic structure of the metal diboride nanosheets, we carried out aberration-corrected high-resolution TEM studies of HfB2. Figure 4A shows a multilayer HfB2 flake composed of four-five layers. There are some smaller domains of different periodicities, which we attribute to smaller flakes of HfB2 restacking onto the larger flake at different crystal alignments. Imaging of the same sample at increased magnification in the region marked by a square (Figure 4B) revealed the hexagonal structure of the HfB2, similar to that of the bulk crystal form. For more detailed comparison with bulk HfB2, we conducted electron scattering simulation using the multislice method<sup>61,62</sup> to simulate the expected HRTEM image of HfB2, with the simulation parameters corresponding to the experimental imaging conditions. We found that the experimental images closely match the simulated structure viewed along the [001] direction (Figure 4B,C). Additional HRTEM images and EELS spectra of MgB2 are shown in the Supporting Information (Figure S7). Calculated geometrical parameters using DFT simulations including vdW interactions (see the Methods section for details) of MgB2 and HfB2 layers of different thicknesses are shown in Table S2 in the Supporting Information. The experimental HRTEM images showed {100} lattice spacing of MgB2 and HfB2 spacings of  $2.68 \pm 0.05$  and  $2.72 \pm 0.05$  Å, respectively. After converting these lattice spacings to the metal-metal bond lengths, we find Mg-Mg and Hf-Hf bond lengths of 3.09 and 3.14 Å, respectively, that are in good agreement with the DFT calculated values (see calculations in the Supporting Information and data in Table S3). It is also worth mentioning that the phonon dispersion for the exfoliated layers does not show any imaginary or soft modes that could compromise the integrity of the structure (Figure S10). This indicates a robust stability for the nanosheets.

Compositional Analysis of  $MB_2$  Nanosheets. EELS was used to identify the elemental makeup of the solution-dispersed metal diborides. The B K-edge for  $HfB_2$  in Figure

4D shows the characteristic peaks of diboride. The peak at 188 eV corresponds to the transitions to the  $\pi^*$  antibonding state, which originates from the sp<sup>2</sup> bonding present within the boron layers. The broad peak centered at 196 eV can be associated with the transitions to the  $\sigma^*$  antibonding orbitals.<sup>63</sup> In Figure 4E, the broad peak above 1600 eV corresponds to the Hf M-edge confirming the presence of Hf.<sup>64</sup> Furthermore, quantitative composition analysis based on the spectra containing B and Hf edges shows the Hf:B ratio to be about 1:2.09, which is very close to the expected value of 1:2 (see Supporting Information, Figure S6). These results show that the chemical composition of pristine HfB2 is generally maintained after solution-phase exfoliation, although there is a small degree of oxidation, which is also shown in the energydispersive X-ray spectroscopy (EDS) spectrum in Figure S6 and the FTIR spectra of MgB2 and CrB2 in Figure S15, which show small B-O and B-OH vibrations that are likely due to some surface oxidation. These EELS spectra were taken at multiple locations on the nanosheet, and little to no spatial variations were found. We also carried out similar atomic structural and compositional analyses of MgB2 sheets as described in the Supporting Information, Figure S7. Calculated EELS spectra for bulk and monolayer MgB<sub>2</sub> (Figures S11 and S12) have features that agree qualitatively with the experimental results.

Synthesis and Mechanical Testing of CrB<sub>2</sub>/PVA Composites. While structures based on metal diboride compounds are conventionally processed at very high temperatures, 1,65 we use liquid-phase exfoliation to produce dispersions that can be incorporated into polymer composites at room temperature. Furthermore, it produces few-layer-thick metal diboride nanosheets that are likely substantially less brittle than their bulk counterparts. As a demonstration of the utility of this scalable sample preparation method, we directly integrated the exfoliated nanosheets into polymer composites using the commonly used and water-soluble matrix PVA. 2D materials have been extensively studied as filler materials for mechanical reinforcement of polymers, with PVA as a commonly chosen polymer because of its ease of processing and compatibility with liquid-phase exfoliated dispersions. Graphene in particular has attracted considerable interest as a result of its remarkable strength and stiffness.<sup>66</sup> The exceptional mechanical properties of the bulk metal diborides suggest their use as filler materials, provided that they can be processed into suitable forms. We thus screened the metal diborides to determine which could produce stable dispersions through direct bath sonication in 1% w/v aqueous PVA. We note that direct bath sonication in water was also performed, yielding stable dispersions of varying concentrations (see Supporting Information, Figure S17). We found that CrB<sub>2</sub> produced the most stable and highest concentration dispersions in PVA. CrB<sub>2</sub> also has good wear resistance, <sup>14</sup> high hardness, high melting point (2200 °C), and high performance under extreme temperature and pressure conditions.<sup>67</sup> These bath-sonicated CrB<sub>2</sub>/PVA dispersions were concentrated and formed into films by a casting process (see the Methods section for more details). The dilution ratio was varied to obtain composites with different mass fractions of CrB2. XRD spectra of the CrB2/PVA composite films have only peaks from PVA and none from the bulk CrB2 phase, suggesting good incorporation of the CrB2 nanosheets, as shown in the Supporting Information (Figure S8). The mechanical properties of multiple composite membranes

were measured by tensile testing (see the **Methods** section for more details).

The polymer composites remained quite flexible with the addition of  $CrB_2$  from 0.13 to 0.27% w/w loadings, as shown in the photograph in Figure 5B. Representative stress—strain

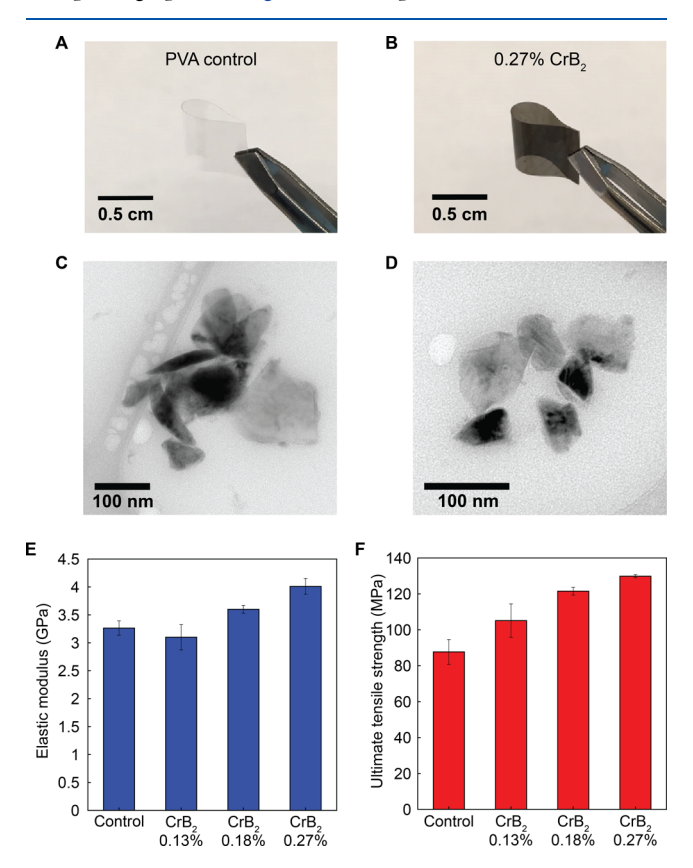


**Figure 5.** Polymer composites and mechanical properties. (A) and (B) Photographs of flexible PVA film (A) and PVA film containing  $\sim\!0.27\%$  CrB $_2$  (B). (C) and (D) Representative TEM images of CrB $_2$  nanosheets dispersed in PVA. (E) Elastic modulus (E) for PVA control with no CrB $_2$  and with CrB $_2$  of different loadings. (F) UTS values for PVA control with no CrB $_2$  and with CrB $_2$  of different loadings.

curves for PVA alone and CrB<sub>2</sub>/PVA composites are shown in the Supporting Information, Figure S9. After measuring the mechanical properties from multiple samples, we found that the CrB<sub>2</sub>/PVA composites with up to 0.27% of CrB<sub>2</sub> showed increases in the elastic modulus and UTS of up to 23 and 48%, respectively. Comparisons of the mechanical properties of the CrB<sub>2</sub>/PVA composites to results from the literature for PVA composites reinforced by direct incorporation of other 2D materials are shown in the Supporting Information Table S1; our results are similar to the enhancement of mechanical properties seen for conventional 2D materials and carbon nanotubes.  $^{68-72}$  However, when the rates of enhancement of E and UTS as a function of volume fraction of nanosheets are calculated ( $dE/dV_f$  and  $dUTS/dV_f$ ), we find that our  $CrB_2$ / PVA has the highest rates of all the literature comparisons. We find a value of  $dE/dV_f$  of 1134 GPa, while the next closest values are 680 GPa for size-sorted graphene 68 and 670 GPa for size-sorted BN.<sup>72</sup> We find a value of dUTS/d $V_f$  of 65,251 MPa, while the next closest values are 47,000 MPa for size-sorted BN<sup>72</sup> and 29,231 MPa for size-sorted MoS<sub>2</sub>.<sup>71</sup>

#### DISCUSSION

We have demonstrated for the first time the solution-phase dispersion of chemically unmodified quasi-2D nanosheets of eight different metal diborides using ultrasonication-assisted exfoliation of bulk powders. The dispersions of metal diborides have concentrations as high as 2.4 mg mL<sup>-1</sup>. We have found that some solvents are more effective at dispersing certain metal diborides than others (see Figure S1b). We attribute this behavior to variations in the surface energies of the quasi-2D nanosheets depending on their metal composition, which allows some cleavage planes to be better stabilized in some solvents rather than others. For instance, the metal diborides that exhibit the most ionic character, MgB2 and AlB2, exfoliate more effectively in more protic solvents such as EtOH and IPA. For the other MB<sub>2</sub> compositions, however, there is a general preference for either ACT or ACN. The MB2 compositions with smaller atomic number metals seem to exfoliate more readily in general. The preference of MgB<sub>2</sub> and AlB, for more protic solvents suggests that the ability to form certain polar interactions with such solvents (e.g., hydrogenbonding) may play an important role in exfoliation and stabilization. In addition to the results shown, it is important to note that the metal diborides in general cannot be exfoliated successfully in very nonpolar solvents such as hydrocarbons, suggesting that some polarity is necessary for exfoliation.

One way of investigating the above observations further is by using a large number of solvents with different characteristics to exfoliate these metal diboride nanosheets and analyze how well each solvent performs, as we have recently done. 54 This analysis determines a metal diboride nanosheet's Hansen solubility parameters, which can provide a metric for determining the suitability of a given exfoliation solvent.<sup>73</sup> Another important factor that influences the formation of metal diboride nanosheets is the breaking of bonds in these nonvdW materials during sonication-assisted cleavage, likely resulting in dangling bonds that can react with their environment. Indeed, some evidence of oxidation in the form of B-O and B-OH bonds is seen in FTIR spectra. The surface chemistry of the metal diboride nanosheets is expected to be more complex than nanosheets from conventional vdW layered materials and should be investigated in more detail in the future. Another interesting observation is that some materials where some similarity may be expected because of similar chemistry and atomic radii, such as Hf and Br, and Nb and Ta, have slightly different exfoliation behaviors in different solvents for their respective diborides. We speculate that subtle differences in bond strength, in the formation of surface reactions with dangling bonds upon exfoliation, and the polarity and chemical nature of the resulting reconstructed surfaces may result in overall differences in exfoliation in different solvents. Further experimental and theoretical investigations will be needed to fully uncover the underlying mechanisms.

TEM and AFM imaging were used to confirm the 2D nature of the resulting nanomaterials, showing thin sheet morphologies with lateral dimensions ranging from 100 nm to multiple microns and thicknesses down to 2–3 nm, although there is a distribution of dimensions. Histograms of the TEM and AFM images show this distribution of flake sizes and thicknesses for different metal diboride compositions, which may indicate differences in metal—boron bond strengths. There are also shifts in the distribution of flake areas as a function of

centrifugation time, suggesting possible routes for future size sorting of the flakes or other changes in the sonication duration and power to achieve thinner flakes, 74–76 which has been shown to improve mechanical properties of polymer nanocomposites of other 2D materials. 68,77 We have observed a trend of thicker and larger flakes being associated with metal diborides with higher values of hardness in the bulk (see Supporting Information, Figure S16 and Table S4), suggesting some correlation with the mechanical properties and bonding. It is also possible that differences in the initial powder particle sizes in the source materials may contribute to the final flake sizes after exfoliation (see detailed mesh sizes of starting materials in the Supporting Information).

HRTEM and EELS were used to show that the crystal lattice and chemical composition are preserved after exfoliation. DFT calculations of phonon dispersions of different layer thicknesses show stability for atomically thin layers of MgB<sub>2</sub>. Harnessing the enhanced processability and increased flexibility of the metal diboride nanosheets, we prepared polymer composites with as-exfoliated CrB2, which resulted in increases in the mechanical strength of the PVA. We found that our nanocomposites had comparable overall enhancements in elastic modulus and UTS as other 2D materials in the literature and even better performance in terms of the rate of enhancement as a function of volume fraction, but without needing to use size sorting methods to find larger sheets. The intrinsic nature of the CrB2 nanosheets, which have high mechanical stiffness and no interlayer slippage issues, as well as possible surface chemical linkages with the surrounding PVA matrix, all contribute to this performance. Moving forward, there are many previously reported strategies for polymer nanocomposites that incorporate carbon nanotubes and graphene oxide such as in situ chemical cross-linking and alignment of the nanoparticle inclusions that can be exploited to achieve even higher enhancements in mechanical properties. 78-

These results represent an important step in the solutionphase, low-temperature processing of UHTCs and open the door to taking advantage of the entire class of metal diboride materials in previously unexplored contexts. The bonding character of metal diborides is different from the layered materials that are related to most conventional 2D materials, which generally possess weak vdW forces between layers. In the metal diborides, boron atoms serve as electron acceptors and metal atoms behave as electron donors; this donoracceptor interaction introduces the ionic character in the M-B bond. However, partial interaction of d-electrons and the formation of spd-hybrid configurations impart a covalent character to the M-B bond leading to a complex bonding environment. The ability to exfoliate these compounds by breaking their mixed character bonds represents a key advancement in our ability to prepare 2D materials from compounds possessing strong interlayer bonding rather than weak vdW bonding. The production of 2D nanosheets from exfoliation of non-vdW precursor solids has recently been demonstrated for the natural ores hematite (Fe<sub>2</sub>O<sub>3</sub>)<sup>81</sup> and ilmenite (FeTiO<sub>3</sub>)<sup>82</sup> and represents a relatively unexplored area for identifying novel low-dimensional materials. These 2D nanosheets of eight different metal diborides exfoliated into stable, homogeneous, and high-concentration dispersions suggest that this method can be generalized to produce 2D diborides from other metal diboride precursors of similar crystal structure and superhard mechanical strength, 83-86

providing a whole new family of 2D materials with a distinct set of properties. Our approach to achieve these boron-based 2D materials also differs from epitaxially grown borophene layers on metal substrates, which rely on the underlying support and are not freestanding.<sup>87–89</sup>

The direct integration of  $CrB_2$  nanosheets into polymer composites and the resulting mechanical reinforcement highlights the potential for using metal diborides in solution-phase processing, which can take advantage of the wide range of existing methods previously developed for other 2D nanomaterials  $^{75,90-94}$  to enable their use in other formats.  $^{95-99}$  Future work may include investigation of the exfoliation behavior and unique properties of other types of boride compounds,  $^{100,101}$  as well as the use of size sorting techniques to further improve the performance by isolating larger flakes.  $^{68,77}$ 

## ASSOCIATED CONTENT

## **Solution** Supporting Information

The Supporting Information is available free of charge at https://pubs.acs.org/doi/10.1021/acs.jpcc.1c00394.

Additional sample preparation details, additional TEM images and EELS data, XRD spectra, mechanical data, and computational simulation data (PDF)

#### AUTHOR INFORMATION

## **Corresponding Authors**

Elton J. G. Santos — Institute for Condensed Matter Physics and Complex Systems, School of Physics and Astronomy and Higgs Centre for Theoretical Physics, The University of Edinburgh, Edinburgh EH9 3FD, United Kingdom; orcid.org/0000-0001-6065-5787; Email: esantos@ed.ac.uk

Alexander A. Green — Biodesign Center for Molecular Design and Biomimetics, The Biodesign Institute, Arizona State University, Tempe, Arizona 85287, United States; School of Molecular Sciences, Arizona State University, Tempe, Arizona 85287, United States; Department of Biomedical Engineering, Boston University, Boston, Massachusetts 02215, United States; orcid.org/0000-0003-2058-1204; Email: aagreen@bu.edu

Qing Hua Wang — Materials Science and Engineering, School for Engineering of Matter, Transport and Energy, Arizona State University, Tempe, Arizona 85287, United States;
occid.org/0000-0002-7982-7275; Email: qhwang@asu.edu

## Authors

Ahmed Yousaf — Biodesign Center for Molecular Design and Biomimetics, The Biodesign Institute, Arizona State University, Tempe, Arizona 85287, United States; School of Molecular Sciences, Arizona State University, Tempe, Arizona 85287, United States

Matthew S. Gilliam — Biodesign Center for Molecular Design and Biomimetics, The Biodesign Institute, Arizona State University, Tempe, Arizona 85287, United States; School of Molecular Sciences, Arizona State University, Tempe, Arizona 85287, United States

Shery L. Y. Chang — Eyring Materials Center, Arizona State University, Tempe, Arizona 85287, United States; Electron Microscopy Unit, Mark Wainwright Analytical Centre and School of Materials Science and Engineering, University of New South Wales, Sydney NSW 2052, Australia; orcid.org/0000-0001-7514-4584

Mathias Augustin — Institute for Condensed Matter Physics and Complex Systems, School of Physics and Astronomy, The University of Edinburgh, Edinburgh EH9 3FD, United Kingdom

Yuqi Guo – Materials Science and Engineering, School for Engineering of Matter, Transport and Energy, Arizona State University, Tempe, Arizona 85287, United States

Fraaz Tahir – Aerospace Engineering and Mechanical Engineering, School for Engineering of Matter, Transport and Energy, Arizona State University, Tempe, Arizona 85287, United States

Meng Wang — Chemical Engineering, School for Engineering of Matter, Transport and Energy, Arizona State University, Tempe, Arizona 85287, United States

Alexandra Schwindt — Chemical Engineering, School for Engineering of Matter, Transport and Energy, Arizona State University, Tempe, Arizona 85287, United States

Ximo S. Chu — Materials Science and Engineering, School for Engineering of Matter, Transport and Energy, Arizona State University, Tempe, Arizona 85287, United States;
ocid.org/0000-0003-2308-6268

Duo O. Li – Materials Science and Engineering, School for Engineering of Matter, Transport and Energy, Arizona State University, Tempe, Arizona 85287, United States

Suneet Kale — Biodesign Center for Molecular Design and Biomimetics, The Biodesign Institute, Arizona State University, Tempe, Arizona 85287, United States; School of Molecular Sciences, Arizona State University, Tempe, Arizona 85287, United States; Materials Science and Engineering, School for Engineering of Matter, Transport and Energy, Arizona State University, Tempe, Arizona 85287, United States

Abhishek Debnath — Biodesign Center for Molecular Design and Biomimetics, The Biodesign Institute, Arizona State University, Tempe, Arizona 85287, United States; School of Molecular Sciences, Arizona State University, Tempe, Arizona 85287, United States

Yongming Liu — Aerospace Engineering and Mechanical Engineering, School for Engineering of Matter, Transport and Energy, Arizona State University, Tempe, Arizona 85287, United States

Matthew D. Green — Chemical Engineering, School for Engineering of Matter, Transport and Energy, Arizona State University, Tempe, Arizona 85287, United States;
orcid.org/0000-0001-5518-3412

Complete contact information is available at: https://pubs.acs.org/10.1021/acs.jpcc.1c00394

#### **Author Contributions**

<sup>‡</sup>A.Y. and M.S.G. contributed equally.

#### **Author Contributions**

M.S.G., A.Y., A.D., and Y.G. performed the solution-phase dispersion experiments. A.Y. and S.L.Y.C. conducted the HRTEM and EELS measurements and electron scattering simulations. M.A. and E.J.G.S. performed the DFT calculations. M.S.G., M.W., A.S., M.D.G., F.T., and Y.L. performed the mechanical testing and analysis. X.S.C., D.O.L., Y.G., and S.K. conducted the AFM imaging. A.Y., Q.H.W., and A.A.G. wrote the manuscript. Q.H.W., A.A.G., and E.J.G.S. directed the project. A.A.G., A.Y., and A.D. have been granted a US

patent related to the results in this manuscript: US 10,711,210 ("Method of preparing metal diboride dispersions and films"), granted July 14, 2020.

#### Notes

The authors declare no competing financial interest. The data that support the findings of this study are available from the corresponding authors upon reasonable request.

## ACKNOWLEDGMENTS

We gratefully acknowledge the use of facilities at the Eyring Materials Center and the W. M. Keck Foundation Laboratory for Environmental Biogeochemistry at ASU and thank Prof. H. Yan for use of his AFM facilities. A.A.G., Q.H.W., A.Y., X.S.C., and M.S.G. were supported by NSF grant DMR-1610153. Q.H.W. was supported by NSF grant DMR-1906030. AAG and QHW also acknowledge startup funds from Arizona State University (ASU). EJGS acknowledges computational resources from CIRRUS Tier-2 HPC Service (ec131 Cirrus Project) at EPCC (http://www.cirrus.ac.uk) funded by the University of Edinburgh and EPSRC (EP/P020267/1); ARCHER UK National Supercomputing Service (http://www.archer.ac.uk) via d429 Project code. EJGS acknowledges the EPSRC Early Career Fellowship (EP/T021578/1) and the University of Edinburgh for funding support. MW and MDG acknowledge funding from ARO (grants W911NF-18-1-0412 and W911NF-15-1-0353).

#### REFERENCES

- (1) Fahrenholtz, W. G.; Hilmas, G. E.; Talmy, I. G.; Zaykoski, J. A. Refractory Diborides of Zirconium and Hafnium. *J. Am. Ceram. Soc.* **2007**, *90*, 1347–1364.
- (2) Heid, R.; Renker, B.; Schober, H.; Adelmann, P.; Ernst, D.; Bohnen, K.-P. Lattice Dynamics and Electron-Phonon Coupling in Transition-Metal Diborides. *Phys. Rev. B* **2003**, *67*, No. 180510.
- (3) Vajeeston, P.; Ravindran, P.; Ravi, C.; Asokamani, R. Electronic Structure, Bonding, and Ground-State Properties of AlB<sub>2</sub>-Type Transition-Metal Diborides. *Phys. Rev. B* **2001**, *63*, No. 45115.
- (4) Post, B.; Glaser, F. W.; Moskowitz, D. Transition Metal Diborides. *Acta Metall.* **1954**, *2*, 20–25.
- (5) Mohammadi, R.; Turner, C. L.; Xie, M.; Yeung, M. T.; Lech, A. T.; Tolbert, S. H.; Kaner, R. B. Enhancing the Hardness of Superhard Transition-Metal Borides: Molybdenum-Doped Tungsten Tetraboride. *Chem. Mater.* **2016**, *28*, 632–637.
- (6) Knyshev, E. A.; Novgorodtsev, V. M.; Plyshevski, U. S.; Kobyakov, V. A.; Stepanova, Z. G.; Svistunov, V. V.; Becketov, A. R. Synthesis of Transition Metal Borides and Their Properties. *J. Less Common Met.* **1976**, *47*, 273–278.
- (7) Fahrenholtz, W. G.; Hilmas, G. E. Ultra-High Temperature Ceramics: Materials for Extreme Environments. *Scr. Mater.* **2017**, *129*, 94–99.
- (8) Wuchina, E.; Opila, E.; Opeka, M.; Fahrenholtz, B.; Talmy, I. UHTCs: Ultra-High Temperature Ceramic Materials for Extreme Environment Applications. *Electrochem. Soc. Interface* **2007**, *16*, 30–36.
- (9) Silvestroni, L.; Kleebe, H.-J.; Fahrenholtz, W. G.; Watts, J. Super-Strong Materials for Temperatures Exceeding 2000 °C. Sci. Rep. 2017, 7, No. 40730.
- (10) Munro, R. G. Material Properties of Titanium Diboride. J. Res. Natl. Inst. Stand. Technol. 2000, 105, 709–720.
- (11) Jordan, L. R.; Betts, A. J.; Dahm, K. L.; Dearnley, P. A.; Wright, G. A. Corrosion and Passivation Mechanism of Chromium Diboride Coatings on Stainless Steel. *Corros. Sci.* **2005**, *47*, 1085–1096.
- (12) Monticelli, C.; Zucchi, F.; Pagnoni, A.; Dal Colle, M. Corrosion of a Zirconium Diboride/Silicon Carbide Composite in Aqueous Solutions. *Electrochim. Acta* **2005**, *50*, 3461–3469.

- (13) Hu, P.; Wang, Z. Flexural Strength and Fracture Behavior of ZrB2–SiC Ultra-High Temperature Ceramic Composites at 1800°C. *J. Eur. Ceram. Soc.* **2010**, *30*, 1021–1026.
- (14) Bhatt, B.; Murthy, T. S. R. C.; Limaye, P. K.; Nagaraj, A.; Singh, K.; Sonber, J. K.; Sairam, K.; Sashanka, A.; Rao, G. V. S. N.; Rao, T. S. Tribological Studies of Monolithic Chromium Diboride against Cemented Tungsten Carbide (WC–Co) under Dry Condition. *Ceram. Int.* **2016**, *42*, 15536–15546.
- (15) Kinoshita, H.; Otani, S.; Kamiyama, S.; Amano, H.; Akasaki, I.; Suda, J.; Matsunami, H. Zirconium Diboride (0001) as an Electrically Conductive Lattice-Matched Substrate for Gallium Nitride. *Jpn. J. Appl. Phys.* **2001**, *40*, L1280–L1282.
- (16) Li, Q.; Zou, X.; Ai, X.; Chen, H.; Sun, L.; Zou, X. Revealing Activity Trends of Metal Diborides Toward pH-Universal Hydrogen Evolution Electrocatalysts with Pt-Like Activity. *Adv. Energy Mater.* **2019**, *9*, No. 1803369.
- (17) Buzea, C.; Yamashita, T. Review of the Superconducting Properties of MgB<sub>2</sub>. Supercond. Sci. Technol. **2001**, 14, R115.
- (18) Kang, W. N.; Kim, H.-J.; Choi, E.-M.; Jung, C. U.; Lee, S.-I. MgB<sub>2</sub> Superconducting Thin Films with a Transition Temperature of 39 Kelvin. *Science* **2001**, 292, 1521–1523.
- (19) Wu, Y.; Messer, B.; Yang, P. Superconducting MgB<sub>2</sub> Nanowires. *Adv. Mater.* **2001**, *13*, 1487–1489.
- (20) Sciti, D.; Silvestroni, L.; Mercatelli, L.; Sans, J.-L.; Sani, E. Suitability of Ultra-Refractory Diboride Ceramics as Absorbers for Solar Energy Applications. *Sol. Energy Mater. Sol. Cells* **2013**, *109*, 8–16.
- (21) Guo, S.-Q. Densification of ZrB<sub>2</sub>-Based Composites and Their Mechanical and Physical Properties: A Review. *J. Eur. Ceram. Soc.* **2009**, 29, 995–1011.
- (22) Neuman, E. W.; Hilmas, G. E.; Fahrenholtz, W. G. Strength of Zirconium Diboride to 2300°C. J. Am. Ceram. Soc. 2013, 96, 47–50.
- (23) Neuman, E. W.; Hilmas, G. E.; Fahrenholtz, W. G. Elevated Temperature Strength Enhancement of ZrB<sub>2</sub>–30 Vol% SiC Ceramics by Postsintering Thermal Annealing. *J. Am. Ceram. Soc.* **2016**, *99*, 962–970
- (24) Sairam, K.; Sonber, J. K.; Murthy, T. S. R. C.; Sahu, A. K.; Bedse, R. D.; Chakravartty, J. K. Pressureless Sintering of Chromium Diboride Using Spark Plasma Sintering Facility. *Int. J. Refract. Hard Met.* **2016**, *58*, 165–171.
- (25) Sairam, K.; Sonber, J. K.; Murthy, T. S. R. C.; Subramanian, C.; Fotedar, R. K.; Hubli, R. C. Reaction Spark Plasma Sintering of Niobium Diboride. *Int. J. Refract. Hard Met.* **2014**, *43*, 259–262.
- (26) Mazánek, V.; Nahdi, H.; Luxa, J.; Sofer, Z.; Pumera, M. Electrochemistry of Layered Metal Diborides. *Nanoscale* **2018**, *10*, 11544–11552.
- (27) Lim, C. S.; Sofer, Z.; Mazánek, V.; Pumera, M. Layered Titanium Diboride: Towards Exfoliation and Electrochemical Applications. *Nanoscale* **2015**, *7*, 12527–12534.
- (28) Akopov, G.; Yeung, M. T.; Kaner, R. B. Rediscovering the Crystal Chemistry of Borides. *Adv. Mater.* 2017, 29, No. 1604506.
- (29) Pangilinan, L. E.; Turner, C. L.; Akopov, G.; Anderson, M.; Mohammadi, R.; Kaner, R. B. Superhard Tungsten Diboride-Based Solid Solutions. *Inorg. Chem.* **2018**, *57*, 15305–15313.
- (30) James, A. L.; Jasuja, K. Chelation Assisted Exfoliation of Layered Borides towards Synthesizing Boron Based Nanosheets. *RSC Adv.* **2017**, *7*, 1905–1914.
- (31) Das, S. K.; Bedar, A.; Kannan, A.; Jasuja, K. Aqueous Dispersions of Few-Layer-Thick Chemically Modified Magnesium Diboride Nanosheets by Ultrasonication Assisted Exfoliation. *Sci. Rep.* **2015**, *5*, No. 10522.
- (32) Das, S. K.; Jasuja, K. Chemical Exfoliation of Layered Magnesium Diboride To Yield Functionalized Nanosheets and Nanoaccordions for Potential Flame Retardant Applications. ACS Appl. Nano Mater. 2018, 1, 1612–1622.
- (33) Ratnam, D.; Das, S. K.; Jasuja, K. Ionic Liquid Assisted Exfoliation of Layered Magnesium Diboride. *IOP Conf. Ser. Mater. Sci. Eng.* **2017**, 225, No. 012111.

- (34) Gunda, H.; Das, S. K.; Jasuja, K. Simple, Green, and High-Yield Production of Boron-Based Nanostructures with Diverse Morphologies by Dissolution and Recrystallization of Layered Magnesium Diboride Crystals in Water. *ChemPhysChem* **2018**, *19*, 880–891.
- (35) Nishino, H.; Fujita, T.; Yamamoto, A.; Fujimori, T.; Fujino, A.; Ito, S. I.; Nakamura, J.; Hosono, H.; Kondo, T. Formation Mechanism of Boron-Based Nanosheet through the Reaction of MgB<sub>2</sub> with Water. *J. Phys. Chem. C* **2017**, *121*, 10587–10593.
- (36) Nishino, H.; Fujita, T.; Cuong, N. T.; Tominaka, S.; Miyauchi, M.; Iimura, S.; Hirata, A.; Umezawa, N.; Okada, S.; Nishibori, E.; et al. Formation and Characterization of Hydrogen Boride Sheets Derived from MgB<sub>2</sub> by Cation Exchange. *J. Am. Chem. Soc.* **2017**, *139*, 13761–13769.
- (37) Nečas, D.; Klapetek, P. Gwyddion: An Open-Source Software for SPM Data Analysis. Cent. Eur. J. Phys. 2012, 10, 181–188.
- (38) Kresse, G.; Hafner, J. Ab Initio Molecular Dynamics for Open-Shell Transition Metals. *Phys. Rev. B* **1993**, *48*, 13115–13118.
- (39) Kresse, G.; Furthmüller, J. Efficient Iterative Schemes for Ab Initio Total-Energy Calculations Using a Plane-Wave Basis Set. *Phys. Rev. B* **1996**, *54*, 11169–11186.
- (40) Perdew, J. P.; Burke, K.; Ernzerhof, M. Generalized Gradient Approximation Made Simple. *Phys. Rev. Lett.* **1996**, 77, 3865–3868.
- (41) Perdew, J. P.; Burke, K.; Ernzerhof, M. Generalized Gradient Approximation Made Simple [Phys. Rev. Lett. 77, 3865 (1996)]. *Phys. Rev. Lett.* **1997**, 78, No. 1396.
- (42) Blöchl, P. E. Projector Augmented-Wave Method. *Phys. Rev. B* **1994**, *S0*, 17953–17979.
- (43) Kresse, G.; Joubert, D. From Ultrasoft Pseudopotentials to the Projector Augmented-Wave Method. *Phys. Rev. B* **1999**, *59*, 1758–1775
- (44) Grimme, S.; Antony, J.; Ehrlich, S.; Krieg, H. A Consistent and Accurate Ab Initio Parametrization of Density Functional Dispersion Correction (DFT-D) for the 94 Elements H-Pu. *J. Chem. Phys.* **2010**, 132, 154104.
- (45) Togo, A.; Tanaka, I. First Principles Phonon Calculations in Materials Science. Scr. Mater. 2015, 108, 1–5.
- (46) First Principles Methods Using CASTEP. Zeitschrift für Kristallographie Crystalline Materials. 2005, 567. DOI: 10.1524/zkri.220.5.567.65075.
- (47) Nguyen, E. P.; Carey, B. J.; Daeneke, T.; Ou, J. Z.; Latham, K.; Zhuiykov, S.; Kalantar-zadeh, K. Investigation of Two-Solvent Grinding-Assisted Liquid Phase Exfoliation of Layered MoS<sub>2</sub>. *Chem. Mater.* **2015**, 27, 53–59.
- (48) Lam, D.; Chen, K.-S.; Kang, J.; Liu, X.; Hersam, M. C. Anhydrous Liquid-Phase Exfoliation of Pristine Electrochemically Active GeS Nanosheets. *Chem. Mater.* **2018**, *30*, 2245–2250.
- (49) Wang, Y.; Liu, Y.; Zhang, J.; Wu, J.; Xu, H.; Wen, X.; Zhang, X.; Tiwary, C. S.; Yang, W.; Vajtai, R.; et al. Cryo-Mediated Exfoliation and Fracturing of Layered Materials into 2D Quantum Dots. *Sci. Adv.* **2017**, 3, No. e1701500.
- (50) Lotya, M.; King, P. J.; Khan, U.; De, S.; Coleman, J. N. High-Concentration, Surfactant-Stabilized Graphene Dispersions. *ACS Nano* **2010**, *4*, 3155–3162.
- (51) Coleman, J. N.; Lotya, M.; O'Neill, A.; Bergin, S. D.; King, P. J.; Khan, U.; Young, K.; Gaucher, A.; De, S.; Smith, R. J.; et al. Two-Dimensional Nanosheets Produced by Liquid Exfoliation of Layered Materials. *Science* **2011**, *331*, 568–571.
- (52) Khan, U.; O'Neill, A.; Lotya, M.; De, S.; Coleman, J. N. High-Concentration Solvent Exfoliation of Graphene. *Small* **2010**, *6*, 864–871.
- (53) Smith, R. J.; King, P. J.; Lotya, M.; Wirtz, C.; Khan, U.; De, S.; Neill, A. O.; Duesberg, G. S.; Grunlan, J. C.; Moriarty, G.; et al. Large-Scale Exfoliation of Inorganic Layered Compounds in Aqueous Surfactant Solutions. *Adv. Mater.* **2011**, 23, 3944–3948.
- (54) Gilliam, M. S.; Yousaf, A.; Guo, Y.; Li, D. O.; Momenah, A.; Wang, Q. H.; Green, A. A. Evaluating the Exfoliation Efficiency of Quasi-2D Metal Diboride Nanosheets Using Hansen Solubility Parameters. *Langmuir* **2021**, *37*, 1194–1205.

- (55) Eda, G.; Yamaguchi, H.; Voiry, D.; Fujita, T.; Chen, M.; Chhowalla, M. Photoluminescence from Chemically Exfoliated MoS<sub>2</sub>. *Nano Lett.* **2011**, *11*, 5111–5116.
- (56) Bang, G. S.; Nam, K. W.; Kim, J. Y.; Shin, J.; Choi, J. W.; Choi, S.-Y. Effective Liquid-Phase Exfoliation and Sodium Ion Battery Application of MoS<sub>2</sub> Nanosheets. *ACS Appl. Mater. Interfaces* **2014**, *6*, 7084–7089.
- (57) Cai, X.; Jiang, Z.; Zhang, X.; Zhang, X. Effects of Tip Sonication Parameters on Liquid Phase Exfoliation of Graphite into Graphene Nanoplatelets. *Nanoscale Res. Lett.* **2018**, *13*, 241.
- (58) Cao, P.; Xu, K.; Varghese, J. O.; Heath, J. R. The Microscopic Structure of Adsorbed Water on Hydrophobic Surfaces under Ambient Conditions. *Nano Lett.* **2011**, *11*, 5581–5586.
- (59) Xu, K.; Cao, P.; Heath, J. R. Graphene Visualizes the First Water Adlayers on Mica at Ambient Conditions. *Science* **2010**, 329, 1188–1191.
- (60) Bollmann, M. T.; Ochedowski, O.; Schleberger, M.; Reichling, M.; Bollmann, T. R. J. Hydration Layers Trapped between Graphene and a Hydrophilic Substrate. *New J. Phys.* **2014**, *16*, 53039.
- (61) Kirkland, E. J. Advanced Computing in Electron Microscopy; Springer US, 2010. DOI: 10.1007/978-1-4419-6533-2.
- (62) Dwyer, C. Simulation of Scanning Transmission Electron Microscope Images on Desktop Computers. *Ultramicroscopy* **2010**, 110, 195–198.
- (63) Garvie, L. A. J.; Craven, A. J.; Brydson, R. Parallel Electron Energy-Loss Spectroscopy (PEELS) Study of B in Minerals: The Electron Energy-Loss near-Edge Structure (ELNES) of the B K Edge. *Am. Mineral.* 1995, 80, 1132–1144.
- (64) Yang, Y.-Y.; Egerton, R. F. Measurements of Oscillator Strength for Use in Elemental Analysis. *Philos. Mag. Part B* **1992**, *66*, 697–709.
- (65) Monteverde, F.; Bellosi, A.; Scatteia, L. Processing and Properties of Ultra-High Temperature Ceramics for Space Applications. *Mater. Sci. Eng., A* **2008**, 485, 415–421.
- (66) Lee, C.; Wei, X.; Kysar, J. W.; Hone, J. Measurement of the Elastic Properties and Intrinsic Strength of Monolayer Graphene. *Science* **2008**, *321*, 385–388.
- (67) Sonber, J. K.; Murthy, T. S. R. C.; Subramanian, C.; Kumar, S.; Fotedar, R. K.; Suri, A. K. Investigation on Synthesis, Pressureless Sintering and Hot Pressing of Chromium Diboride. *Int. J. Refract. Hard Met.* **2009**, *27*, 912–918.
- (68) May, P.; Khan, U.; O'Neill, A.; Coleman, J. N. Approaching the Theoretical Limit for Reinforcing Polymers with Graphene. *J. Mater. Chem.* **2012**, 22, 1278.
- (69) Liang, J.; Huang, Y.; Zhang, L.; Wang, Y.; Ma, Y.; Guo, T.; Chen, Y. Molecular-Level Dispersion of Graphene into Poly(Vinyl Alcohol) and Effective Reinforcement of Their Nanocomposites. *Adv. Funct. Mater.* **2009**, *19*, 2297–2302.
- (70) Liu, L.; Barber, A. H.; Nuriel, S.; Wagner, H. D. Mechanical Properties of Functionalized Single-Walled Carbon-Nanotube/Poly-(Vinyl Alcohol) Nanocomposites. *Adv. Funct. Mater.* **2005**, *15*, 975–980.
- (71) O'Neill, A.; Khan, U.; Coleman, J. N. Preparation of High Concentration Dispersions of Exfoliated  $MoS_2$  with Increased Flake Size. *Chem. Mater.* **2012**, 24, 2414–2421.
- (72) Khan, U.; May, P.; O'Neill, A.; Bell, A. P.; Boussac, E.; Martin, A.; Semple, J.; Coleman, J. N. Polymer Reinforcement Using Liquid-Exfoliated Boron Nitride Nanosheets. *Nanoscale* **2013**, *5*, 581–587.
- (73) Hernandez, Y.; Lotya, M.; Rickard, D.; Bergin, S. D.; Coleman, J. N. Measurement of Multicomponent Solubility Parameters for Graphene Facilitates Solvent Discovery. *Langmuir* **2010**, *26*, 3208–3213.
- (74) Wang, X.; Bai, H.; Shi, G. Size Fractionation of Graphene Oxide Sheets by pH-Assisted Selective Sedimentation. *J. Am. Chem. Soc.* **2011**, *133*, 6338–6342.
- (75) Green, A. A.; Hersam, M. C. Solution Phase Production of Graphene with Controlled Thickness via Density Differentiation. *Nano Lett.* **2009**, *9*, 4031–4036.

- (76) Green, A. A.; Hersam, M. C. Emerging Methods for Producing Monodisperse Graphene Dispersions. *J. Phys. Chem. Lett.* **2010**, *1*, 544–549.
- (77) Lin, X.; Shen, X.; Zheng, Q.; Yousefi, N.; Ye, L.; Mai, Y.-W.; Kim, J.-K. Fabrication of Highly-Aligned, Conductive, and Strong Graphene Papers Using Ultralarge Graphene Oxide Sheets. *ACS Nano* **2012**, *6*, 10708–10719.
- (78) Wang, Z.; Ciselli, P.; Peijs, T. The Extraordinary Reinforcing Efficiency of Single-Walled Carbon Nanotubes in Oriented Poly-(Vinyl Alcohol) Tapes. *Nanotechnology* **2007**, *18*, No. 455709.
- (79) Coleman, J. N.; Khan, U.; Gun'ko, Y. K. Mechanical Reinforcement of Polymers Using Carbon Nanotubes. *Adv. Mater.* **2006**, *18*, 689–706.
- (80) Zhao, X.; Zhang, Q.; Chen, D.; Lu, P. Enhanced Mechanical Properties of Graphene-Based Poly(Vinyl Alcohol) Composites. *Macromolecules* **2010**, 43, 2357–2363.
- (81) Puthirath Balan, A.; Radhakrishnan, S.; Woellner, C. F.; Sinha, S. K.; Deng, L.; de los Reyes, C.; Rao, B. M.; Paulose, M.; Neupane, R.; Apte, A.; et al. Exfoliation of a Non-van Der Waals Material from Iron Ore Hematite. *Nat. Nanotechnol.* **2018**, *13*, 602–609.
- (82) Puthirath Balan, A.; Radhakrishnan, S.; Kumar, R.; Neupane, R.; Sinha, S. K.; Deng, L.; de los Reyes, C. A.; Apte, A.; Rao, B. M.; Paulose, M.; et al. A Non-van Der Waals Two-Dimensional Material from Natural Titanium Mineral Ore Ilmenite. *Chem. Mater.* **2018**, *30*, 5923–5931.
- (83) Levine, J. B.; Nguyen, S. L.; Rasool, H. I.; Wright, J. A.; Brown, S. E.; Kaner, R. B. Preparation and Properties of Metallic, Superhard Rhenium Diboride Crystals. *J. Am. Chem. Soc.* **2008**, *130*, 16953–16958.
- (84) Lech, A. T.; Turner, C. L.; Lei, J.; Mohammadi, R.; Tolbert, S. H.; Kaner, R. B. Superhard Rhenium/Tungsten Diboride Solid Solutions. J. Am. Chem. Soc. 2016, 138, 14398–14408.
- (85) Chung, H.-Y.; Weinberger, M. B.; Levine, J. B.; Kavner, A.; Yang, J.-M.; Tolbert, S. H.; Kaner, R. B. Synthesis of Ultra-Incompressible Superhard Rhenium Diboride at Ambient Pressure. *Science* **2007**, *316*, 436–439.
- (86) Cumberland, R. W.; Weinberger, M. B.; Gilman, J. J.; Clark, S. M.; Tolbert, S. H.; Kaner, R. B. Osmium Diboride, An Ultra-Incompressible, Hard Material. *J. Am. Chem. Soc.* **2005**, *127*, 7264–7265.
- (87) Mannix, A. J.; Zhou, X.-F.; Kiraly, B.; Wood, J. D.; Alducin, D.; Myers, B. D.; Liu, X.; Fisher, B. L.; Santiago, U.; Guest, J. R.; et al. Synthesis of Borophenes: Anisotropic Two-Dimensional Polymorphs. *Science* **2015**, *350*, 1513–1516.
- (88) Kiraly, B.; Liu, X.; Wang, L.; Zhang, Z.; Mannix, A. J.; Fisher, B. L.; Yakobson, B. I.; Hersam, M. C.; Guisinger, N. P. Borophene Synthesis on Au(111). ACS Nano 2019, 13, 3816–3822.
- (89) Wu, R.; Drozdov, I. K.; Eltinge, S.; Zahl, P.; Ismail-Beigi, S.; Božović, I.; Gozar, A. Large-Area Single-Crystal Sheets of Borophene on Cu(111) Surfaces. *Nat. Nanotechnol.* **2019**, *14*, 44–49.
- (90) Chu, X. S.; Yousaf, A.; Li, D. O.; Tang, A. A.; Debnath, A.; Ma, D.; Green, A. A.; Santos, E. J. G.; Wang, Q. H. Direct Covalent Chemical Functionalization of Unmodified Two-Dimensional Molybdenum Disulfide. *Chem. Mater.* **2018**, *30*, 2112–2128.
- (91) Wang, Q. H.; Shih, C.-J.; Paulus, G. L. C.; Strano, M. S. Evolution of Physical and Electronic Structures of Bilayer Graphene upon Chemical Functionalization. *J. Am. Chem. Soc.* **2013**, *135*, 18866–18875.
- (92) Kaplan, A.; Yuan, Z.; Benck, J. D.; Govind Rajan, A.; Chu, X. S.; Wang, Q. H.; Strano, M. S. Current and Future Directions in Electron Transfer Chemistry of Graphene. *Chem. Soc. Rev.* **2017**, *46*, 4530–4571.
- (93) Wang, Q. H.; Jin, Z.; Kim, K. K.; Hilmer, A. J.; Paulus, G. L. C.; Shih, C.-J.; Ham, M.-H.; Sanchez-Yamagishi, J. D.; Watanabe, K.; Taniguchi, T.; et al. Understanding and Controlling the Substrate Effect on Graphene Electron-Transfer Chemistry via Reactivity Imprint Lithography. *Nat. Chem.* **2012**, *4*, 724–732.
- (94) Seo, J.-W. T.; Green, A. A.; Antaris, A. L.; Hersam, M. C. High-Concentration Aqueous Dispersions of Graphene Using Nonionic,

- Biocompatible Block Copolymers. J. Phys. Chem. Lett. 2011, 2, 1004–1008
- (95) Zhu, C.; Han, T. Y.-J.; Duoss, E. B.; Golobic, A. M.; Kuntz, J. D.; Spadaccini, C. M.; Worsley, M. A. Highly Compressible 3D Periodic Graphene Aerogel Microlattices. *Nat. Commun.* **2015**, *6*, 6962.
- (96) García-Tuñon, E.; Barg, S.; Franco, J.; Bell, R.; Eslava, S.; D'Elia, E.; Maher, R. C.; Guitian, F.; Saiz, E. Printing in Three Dimensions with Graphene. *Adv. Mater.* **2015**, *27*, 1688–1693.
- (97) Fu, K.; Wang, Y.; Yan, C.; Yao, Y.; Chen, Y.; Dai, J.; Lacey, S.; Wang, Y.; Wan, J.; Li, T.; et al. Graphene Oxide-Based Electrode Inks for 3D-Printed Lithium-Ion Batteries. *Adv. Mater.* **2016**, *28*, 2587–2594.
- (98) Li, D.; Müller, M. B.; Gilje, S.; Kaner, R. B.; Wallace, G. G. Processable Aqueous Dispersions of Graphene Nanosheets. *Nat. Nanotechnol.* **2008**, *3*, 101–105.
- (99) Hu, G.; Kang, J.; Ng, L. W. T.; Zhu, X.; Howe, R. C. T.; Jones, C. G.; Hersam, M. C.; Hasan, T. Functional Inks and Printing of Two-Dimensional Materials. *Chem. Soc. Rev.* **2018**, *47*, 3265–3300.
- (100) Yeung, M. T.; Akopov, G.; Lin, C.-W.; King, D. J.; Li, R. L.; Sobell, Z. C.; Mohammadi, R.; Kaner, R. B. Superhard W<sub>0.5</sub>Ta<sub>0.5</sub>B Nanowires Prepared at Ambient Pressure. *Appl. Phys. Lett.* **2016**, *109*, 203107.
- (101) Carenco, S.; Portehault, D.; Boissière, C.; Mézailles, N.; Sanchez, C. Nanoscaled Metal Borides and Phosphides: Recent Developments and Perspectives. *Chem. Rev.* **2013**, *113*, 7981–8065.